Design and prototyping wire arc additively manufactured aluminum alloy lattice structures

Published Version:
Baglivo, L., Avallone, G., Caso, M., D'Arcangelo, S., Benni, A.A., Laghi, V., et al. (2024). Design and prototyping wire arc additively manufactured aluminum alloy lattice structures. INTERNATIONAL JOURNAL, ADVANCED MANUFACTURING TECHNOLOGY, 135(7-8), 3747-3764 [10.1007/s00170-024-14734-x].

Availability:
This version is available at: https://hdl.handle.net/11585/996371 since: 2025-01-22

Published:
DOI: http://doi.org/10.1007/s00170-024-14734-x

(Article begins on next page)

Design and Prototyping Wire Arc Additively Manufactured Aluminum Alloy Lattice Structures

Luca Baglivo[1], Giovanni Avallone[1], Marco Caso[1], Simone D'Arcangelo[2], Akshay Ashok Benni[2], Vittoria Laghi[3], Lidiana Arrè[3], Giada Gasparini[3], Michele Palermo[3], Stefano Petrò[2], Tianqiu Xu[2*], Barbara Previtali[2]

[1]Caracol, Via Marisa Bellisario, 6C, 20825, Barlassina (MB), Italy

[2]Department of Mechanical Engineering, Politecnico di Milano, Via La Masa, 1 - 20156 Milan, Italy

[3]Department of Civil, Chemical, Environmental and Materials Engineering (DICAM), University of Bologna, Viale del Risorgimento, 2 – 40136 Bologna, Italy

**Corresponding author:*

Tianqiu Xu: tianqiu.xu@polimi.it

Abstract

Aluminum alloy lattice structures have important application prospects in modern engineering, construction, and lightweight manufacturing of key industrial components. The current "dot-by-dot" manufacturing method, using Wire Arc Additive Manufacturing (WAAM) with Cold Metal Transfer (CMT) as the heat source is an important way to achieve integrated manufacturing of large-sized and complex aluminum alloy lattice structure. In this paper, a detailed study is conducted on the design and prototype manufacturing of aluminum alloy dot-by-dot deposition process. Single strut design, "X lattice unit" design and geometric parameter design are explored through characterization of both microstructural and mechanical properties. The porosity, microstructure, and mechanical properties of the lattice strut in different areas were studied. The majority of pores were present between each layer deposition and accumulated in the line bridge area. A detailed discussion was then conducted on the formation mechanism of pores in aluminum alloy struts and the deposition strategy of the so-called X lattice unit. Finally, the manufacturing of a circular lattice structure composed of X lattice unit was achieved through deposition strategies control.

Keywords

Wire Arc Additive Manufacturing, lattice structures, Aluminum alloy, Microstructural analysis, Mechanical properties.

1. Introduction

Metal lattice structures have broad application prospects in fields such as construction [1, 2], vehicles [3], and aircraft[3] due to their lightweight and high-strength functional characteristics. However, due to its complex configuration, traditional processing methods for lattice structures have limitations. On the other hand, additive manufacturing (AM) has outstanding advantages and broad application prospects in the manufacturing of lattice structures due to its integrated forming ability with complex configurations. Aluminum alloy is a lightweight metal with low melting point and high thermal conductivity, making it widely applicable in weight reduction of industrial parts, such as aircraft frame[4], turbojet engine blades[5], and hollow components[6]. Aluminum alloy lattice structures combine the excellent material characteristics of aluminum alloy with the functional characteristics of lattice structure. This combination enables further lightweight manufacturing of parts and offers a very broad application prospect [7, 8]. Compared with traditional machining techniques, its characteristics enable it to have the ability to fabricate complex spatial structures, thus gradually becoming the most suitable manufacturing method for various types of lattice structures.

Today the most established process for obtaining lattice structures and fine features is the powder bed process, mainly laser powder bed fusion (LPBF) [9-11] and Electron Beam Powder Bed Fusion (EBPBF) [12-14]. Both LPBF and EBPBF have the unique advantage in manufacturing lattice structures due to the characteristic of small size of spot, the thin layer thickness. These characteristics and advantages are not present in Directed Energy Deposition (DED) processes, but it is worth noting that in recent years, DED has gradually been applied to manufacture lattice structures, especially large-sized metal truss structures [7, 15, 16]. Although there is some literature evidence of lattice structures obtained with laser metal deposition (LMD) [17], they are mainly manufactured through Wire Arc Additive Manufacturing (WAAM) processes. According to the different types of heat source and deposition mode of the WAAM, it can be referred to either Gas Tungsten Arc Welding (GTAW)[18-20], Plasma Arc Welding (PAW)[21, 22], Gas Metal Arc Welding (GMAW)[23, 24] or Cold Metal Transfer (CMT)[25, 26]. This technology has recently been intensively studied for producing wall structures from various alloys such as Al-alloys, Mg-alloys, stainless steels and Ni-based superalloys[27-35]. In the GTAW process, the heat source is stable due to the use of side-axis wire feeding, which is conducive to reducing spatter, but it is currently difficult to finely control the heat input. GMAW uses a coaxial wire feeding mode, the metal wire is both the heat source and the material, which has a higher deposition efficiency, but the droplet transition is more sensitive and prone to spatter. PAW is suitable for precise and fine deposition due to the concentrated arc, and has higher deposition accuracy, but the overall deposition efficiency for large-scale structures is low.

CMT is a variant of GMAW that offers controlled heat input by intermittently pulling back the wire, reducing spatter and heat distortion[36, 37].

Presently, WAAM is the predominant method for fabricating lattice structures within all various DED processes [38-43]. This is due to its capability to employ a so-called “dot-by-dot” printing strategy, which offers precision and control of the material drop and consequent thermal load[38, 39]. In detail, the dot-by-dot printing strategy consists of layering subsequent drops of molten metal to create bar-like and lattice parts [39].

Metal lattice structures fabricated by WAAM have gradually become a research hotspot, as shown in Table 1. Compared with other AM methods (such as LPBF), it uses an arc as the heat source and metal wire as the material, which melts through the metal wire and deposits droplets dot by dot. At present, the metal lattice structures manufactured by WAAM mainly include stainless steel, titanium alloys, aluminum alloys. Researcher effort was primarily focused on the mechanical characterization and design developments, with special effort on features like material properties, manufacturing characteristics, and architectural design. Radel et al. [44] used the WAAM-CMT method to manufacture spatial bars and proposed a manufacturing strategy for dot-by-dot automatic manufacturing of complex spatial truss structures using Computer Aided Manufacturing (CAM) technology. Silvestru et al. [45] achieved WAAM of stainless steel metal rods through a multi axis welding robot by employing the so-called “point-by-point” strategy (assimilated as dot-by-dot). Laghi et al. [38, 39] explored a novel unsupported WAAM technology for manufacturing stainless steel lattice structures, which can be applied in the construction field. Wang et al. [46] also studied the forming process of spatial bar structures using the WAAM-GMAW (CMT) method. Their investigation encompassed several key components, such as point-by-point deposition manufacturing strategy, mechanical analysis model in WAAM, path optimization method, and interference adjustment strategy based on collision detection method. Wu et al. [47] also conducted multiple explorations in the field of spatial member structure manufacturing. For this aim, the team proposed a Skeleton Arc Additive Manufacturing (SAAM) for skeletal structures. Xu et al. [41-43] used the WAAM-GTAW method to manufacture unsupported spatial rod structures and achieved multi angle spatial rod unsupported manufacturing from 0 ° to 90 °. Y. Li et al. [7] used the WAAM-GMAW (CMT) method to manufacture aluminum alloy multi angle tilted rods and large multi-layer lattice structures using a multi axis welding robot. Yu et al.[8, 16, 48] achieved the manufacturing of aluminum alloy pyramid lattice using the WAAM-GMAW (CMT) method based on the manufacturing of suspended rod structures. Abe et al. [15] studied the influence of process parameters on the macroscopic morphology of formed specimens during the manufacturing of spatial rods, and ultimately achieved the manufacturing of multi-layer pyramid lattice structures. Zheng et al. [49, 50]explored the detailed fabrication mechanism and microstructure and properties of aluminum alloy lattice structure as well as the curved-generatrix-shell pyramid lattice structure by WAAM-CMT.

It can be seen that through the exploration of lattice structure AM technology, the current WAAM process can achieve preliminary metal lattice structure deposition. However, due to the low melting point and high thermal conductivity of aluminum alloys, controlling heat input is one of the research difficulties in subsequent WAAM processes. At present, the analysis of WAAM dot-by-dot deposition process for aluminum alloy is still not systematically conducted. The research on internal pores defects, microstructures, and mechanical properties of different forms of dot-by-dot aluminum alloy strut samples lacks comprehensive coverage.

This paper investigates WAAM aluminum lattice structures fabricated by CMT method and dot-by-dot technique. The fabrication process involved designing the geometric parameters of a single droplet, designing the deposition path, and exploring the manufacturing process through experiments. Furthermore, the macroscopic and microscopic morphology of the strut at different positions was characterized and internal defects were detected and analyzed using X-ray Computed Tomography (XCT). The study also explored the mechanisms of porosity formation in the dot-by-dot process for creating aluminum alloy struts. Finally, the microhardness and tensile properties of different rods were compared, resulting in a detailed and comprehensive exploration of deposition strategies and design for aluminum alloy lattice structure. Notably, this study further investigated the manufacturing of both “X lattice unit” and lattice structure, particularly focusing on the manufacturing strategy of joint areas and analyzes the effects of the different shapes of the joint area.

Table 1 A summary of literature state of art on lattice structure fabricated by WAAM

	WAAM-GTAW	WAAM-CMT
Equipment	Machine tool [41, 42, 51]	Machine tool [8, 16] Robot [7, 15, 38, 39, 45, 47, 48]
Methodology	Dot-by-dot [41, 42, 51]	Dot-by-dot [16, 48-50]
Lattice types	Pyramid lattice [41-43, 51] Inclined rod [41-43, 51]	Pyramid lattice [8, 16, 46, 48-50] Inclined rod [7, 8, 16, 38, 46, 49, 50] Curve rod [8] Kagome lattice [15] Spatial other types [8, 16, 38]

Materials	Stainless steel [51, 52] Titanium alloy [41-43]	Aluminum alloy [7, 8, 16, 48-50] Stainless steel [15, 46]

2. Experimental tests

2.1 Materials and Process

Commercially available ER2319 aluminum welding wire of nominal diameter 1.2 mm supplied by Bohler (Vienna, Austria) was used as feedstock wire, and a 20-mm thick Al5083 (AlMg4.5Mn) block was used as substrate. The nominal chemical composition of the wire feedstock is seen in Table 2.

Table 2: Nominal chemical composition of feedstock wire (wt%)

Al	Mg	Ti	V	Mn	Cu	Zr
Bal.	<0.02	0.1-0.2	0.05-0.15	0.2-0.4	5.8-6.8	0.10-0.25

The WAAM system was established at Caracol AM SRL (Barlassina, Italy) [64]. The schematic diagram of the manufacturing system is shown in Fig.1(a), using a welding robot as the main carrier for WAAM. The system comprises a six-axis robotic arm (KR 12, KUKA, Augsburg, Germany) and a Gas Metal Arc Welding (GMAW) setup provided by Fronius (Pettenbach, Austria), which included a power source, rear wire feeder, torch wire feeder, and a welding torch, as shown in Fig.1(b). A software framework consisting of a 3D modeling package Rhinoceros3D with Grasshopper extension was used to program the deposition path.

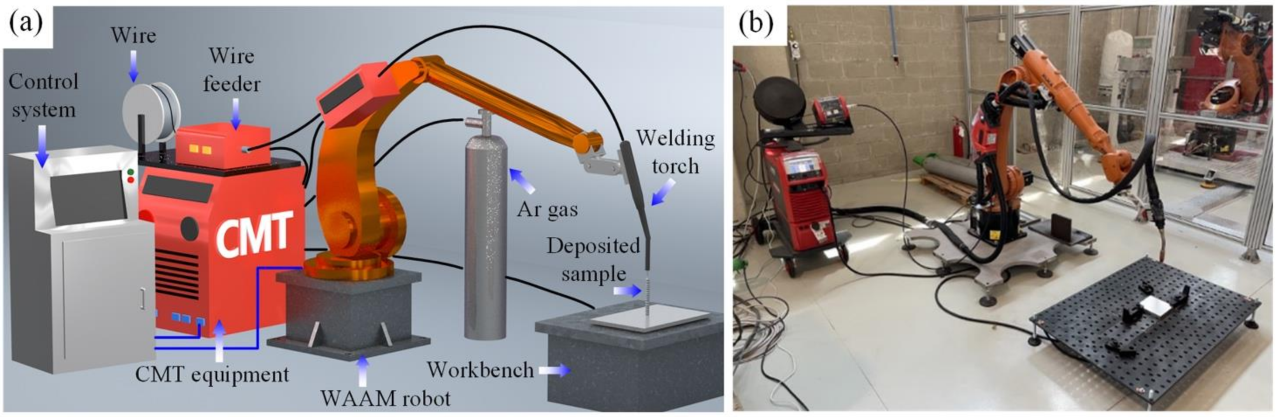

Fig.1 WAAM system and equipment: (a) Schematic diagram of WAAM equipment. (b) Photo of WAAM equipment of Caracol

2.2 Experimental design

Single struts of 5-mm nominal diameter and 210-mm height were deposited with the dot-by-dot deposition strategy, as seen in Fig.2(a). The process parameters utilised in this study were determined based on preliminary experiment exploration. These parameters were then adjusted to align with the point-wise deposition strategy employed in this study, as shown in Table 3. The Cold Metal Transfer (CMT) module was used, and the process parameters were fixed during the deposition: the wire feed rate was set at 2.7 m/min, voltage and current maintained at 10.8 V and 41 A respectively, and the stand-off distance (the distance between the torch tip and substrate) was held at 15 mm. Additionally, 99.99% pure Argon was used as shielding gas with a flow rate of 16 l/min. In a dot-by-dot strategy, the critical parameter is the "arc-on" time which governs the drop dimension. For the single strut in Fig.2(a), after preliminary experiments (not reported for the sake of brevity) the arc-on time was set to 0.5 seconds. In the case of the columnar lattice structure in Fig.2(b), the arc-on time was set to 0.8 seconds for the cross joint and 0.5 seconds for all the remaining parts. Consequently, the nominal drop diameter and height of the single strut in Fig.2(a) were equal to 5 mm and 1 mm, respectively, while the drop height (hence the layer height for dot-by-dot process) was equal to 1.3 mm in the case of the columnar lattice structures. Before analysing the microstructure and mechanical properties of the specimens, the density of the single struts was evaluated.

Following the study of the single strut, the columnar lattice structure in Fig.2(b) was then deposited. The fundamental lattice unit of the columnar structure is shown in Fig.2(b). The unit cell can be regarded as "X lattice unit", formed by two distinct inclined rods meeting at a cross joint, as depicted in Fig.2(c). This cross joint can be visualised as a cluster of different droplets. It should be noted that the building direction was kept always vertical (i.e. the welding torch was always perpendicular with respect to the substrate, as shown in Fig.2(a)).

Table 3: Process parameters employed for the dot-by-dot lattice manufacturing

Parameter	Value
Wire feed rate, m/min	2.7
Current, A	41
Voltage, V	10.8
Stand-off distance, SOD, mm	15
Shielding gas	Argon
Shielding Gas flow rate, l/min	16

Arc on time, s (in Fig.2 (a))	0.5
Arc on time, s (in Fig.2 (b), cross joint dot, in blue)	0.8
Arc on time, s (in Fig.2 (b), except for cross joint dot)	0.5
Arc wait time, s (in Fig.2 (a))	15
Arc wait time, s (in Fig.2 (b))	10
Nominal layer height, h, mm (in Fig.2(a))	1
Nominal layer height, h, mm (in Fig.2(b))	1.3
Nominal bead diameter, d, mm (in Fig.2)	5

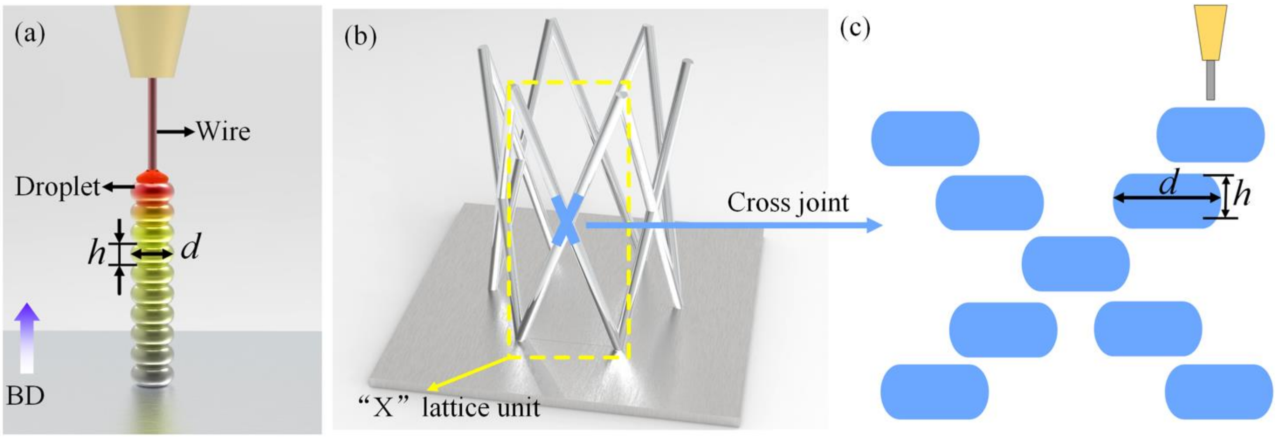

Fig.2 Design of the experimented lattice unitary geometries: (a) single strut, (b) columnar lattice structure and single lattice unit of the lattice columnar structure, (c) cross joint located at the intersection of the "X lattice unit".

3. Material characterization

3.1 Microstructure characterization

For the microstructure analysis, the longitudinal cross-section of the single strut was considered. Initially, the single strut was cut into two parts along its central axis, as illustrated in Fig.3(a). Subsequently, one half of the metal strut was further divided for metallographic observation into three sub-sections (namely the top, the middle and the bottom sections) measuring 30 mm each, as shown in Fig.3 (b). These cross-sections were then prepared by grinding with 180, 320, 600, 800, 1200, and 2500 abrasive papers respectively, followed by polishing with 6 μm, 3 μm, and 1 μm diamond paste.

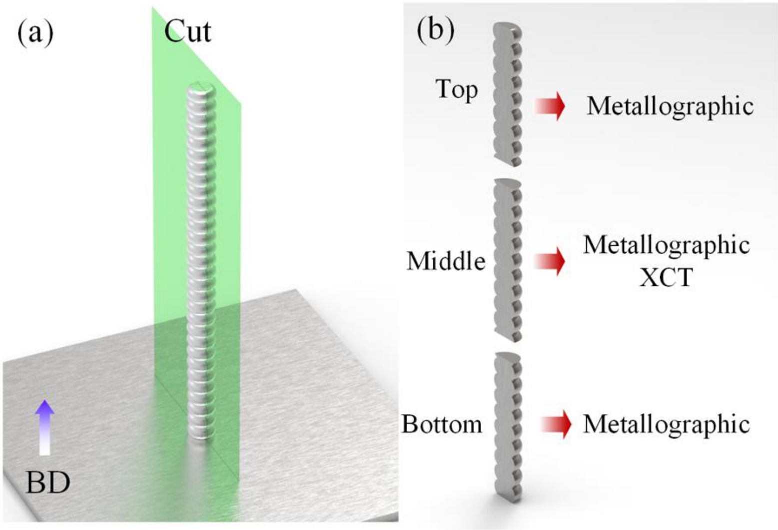

Fig.1: Preparation of single strut for metallographic analysis: (a) cross section plane, (b) three regions of the single strut used for metallographic and XCT characterization.

Porosity and microstructure analysis were conducted on the polished cross-sections obtained using an optical microscope (Leitz Ergolux 200). ImageJ software (U.S. National Institutes of Health, Bethesda, Maryland, USA) was employed to calculate porosity. Chemical etching was performed with Keller's solution (95% H_2O, 2.5% HNO_3, 1.5% HCl, and 1% HF). To obtain a comprehensive 3D characterization of the internal structure of the samples, two X-ray computed tomography (XCT) scans were conducted. The first scan aimed to characterize the porosity distribution within the single strut, employing high magnification acquisition. The second scan focused on characterizing the global distribution of porosity within the lattice structure. The NSI X25 XCT scanner (Nort Star Imagining, USA) was used with the scan parameters detailed in Table 4. Subsequently, the acquired images were analysed using VGStudio Max 3.4 (Volume Graphics, USA).

Table 4: Scan parameters employed for acquisitions of images for XCT.

Parameter	Value
Voltage, kV	100
Current, μA	25-40
Acquisition, FPS	5-15
No. of averaged images	10
No. of projections	2000
Physical filter, mm	1.3 Al

Magnification-strut, X	2.2
Magnification-lattice, X	13.5
Physical pixel size, µm	75
Voxel size-strut, µm	34
Voxel size-lattice, µm	5.7
Image size-strut, voxel	1706x1522x2804
Image size-lattice, voxel	1021x1014x1238

3.2 Mechanical characterization

Vickers hardness analysis was conducted on the polished cross-section under a loading of 200GF and dwell time of 15 s using a microhardness indenter (MH3, Metkon®, Bursa, Turkey) in accordance with ASTM E384 − 17 standard. Tensile tests were carried out on the as-deposited strut using a universal testing machine with 500 kN load capacity.

The tensile specimens, as depicted in Fig.4, were tested under displacement control with a loading rate of 2 MPa/s. In this study, two types of tensile specimens were tested.

A first batch of specimens were tested with as-built geometry without machining processing as shown in Fig.4(a), to assess the mechanical performances of the tested parts accounting for the inherent geometrical irregularities typical of the dot-by-dot process. From these tests, the key mechanical properties were extracted as effective properties, i.e. considering the volume-equivalent (or effective) cross-sectional area, as also applied in [39, 53].

A second batch of specimens were tested on machined samples to avoid the effect of the geometrical irregularities and hence capture the essential mechanical properties (Fig.4(b)). Machined samples were fabricated by CNC lathes and milling machines.

The tests were carried out using a Universal testing machine with 100 kN load capacity at the Mechanical Engineering Labs at Politecnico of Milan. A linear deform meter (with a nominal length of 50 mm) was also used to detect the global strain of the specimens up to yielding.

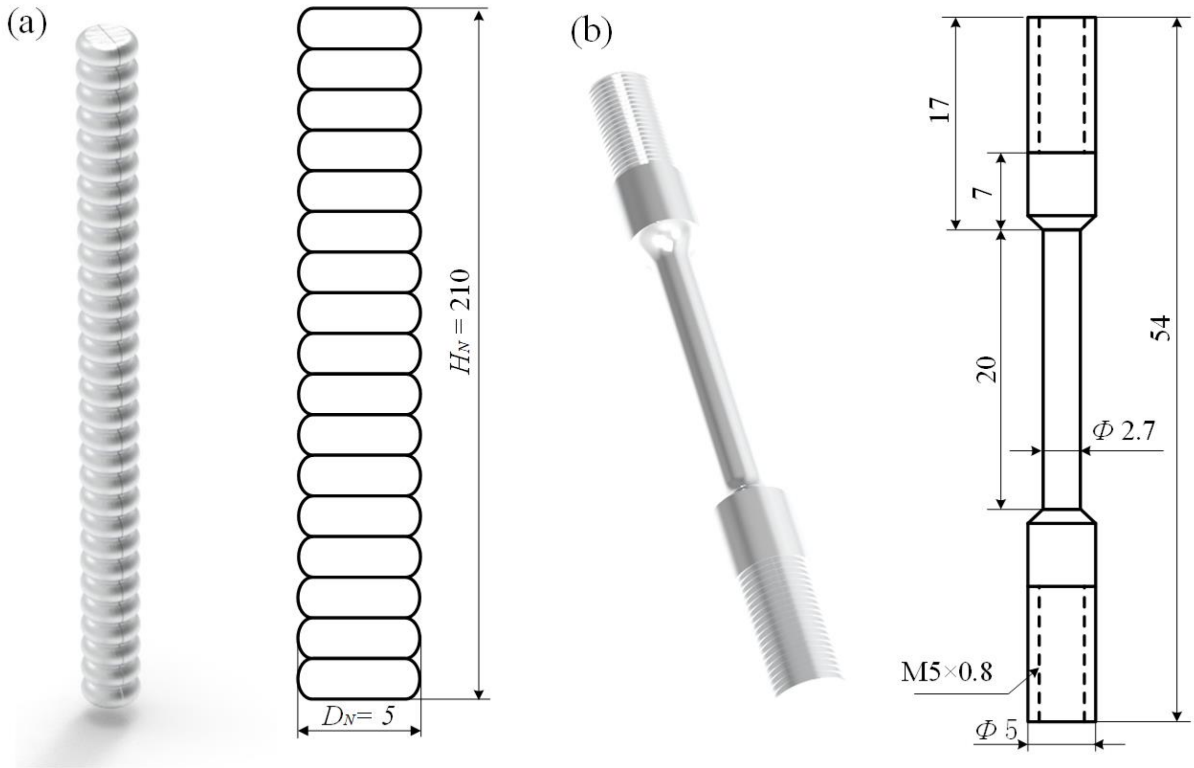

Fig.4 Tensile test specimens: (a) specimen dimensions for as-deposited strut (H_N is the nominal height, D_N is the nominal diameter), (b) specimen dimensions for machined strut.

4. Results and discussion

4.1 Single strut

The deposited single struts, as depicted in Fig.5, exhibited a measured height of 210 mm, with significant variation observed in the cross-section, as expected in the deposition employing dot-by-dot strategy. As shown in Fig.5, for the as-built tests, three of the single struts (number 1-3 in Fig.5) were utilized. Additionally, one strut was machined to obtain three tensile test samples (number 4), while the remaining one (number 5) was used for density and microstructural characterization.

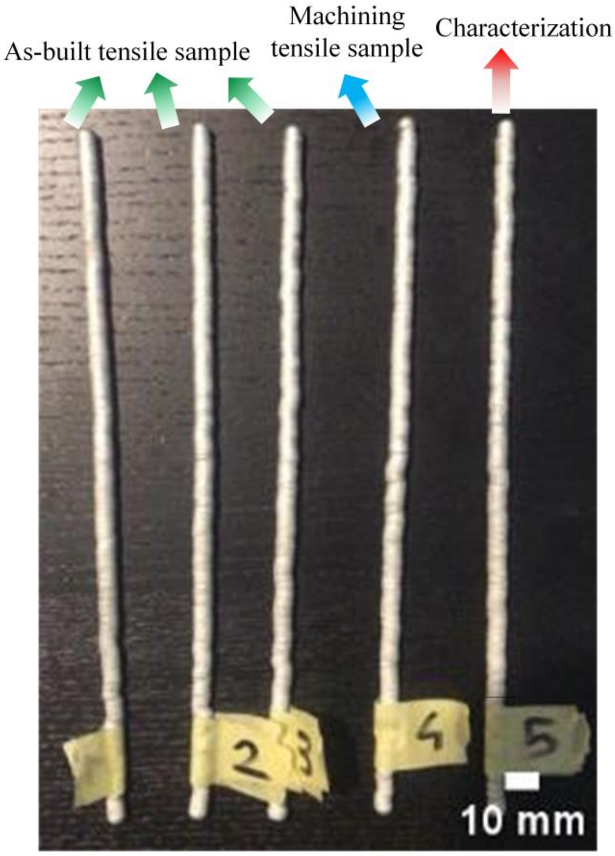

Fig.5 Single struts deposited with WAAM

4.2 Porosity analysis

The cross-section acquisitions of the three regions of the single struts captured by an optical microscope are shown in Fig.6. Higher porosity was observed in the top section, while the lowest one was in the bottom region, with the overall porosity of the entire strut being on average 1.6 ± 0.8 %. In order to further analyze the distribution of pores and clarify the morphology and number of pores, XCT was used to characterize the pores of the strut sample.

The XCT image underwent thorough analysis to determine the distribution and sizes of the pores present. Fig.7(a) shows a single strut sample at high magnification from an XCT image, where individual drops are distinguishable from the alternate dark (low X-ray attenuation) and light layers (high X-ray attenuation). The difference in the X-ray attenuation typically arises from the differences in material composition and crystalline structure. The presence of microporosity further diminishes the attenuation. Fig.7(b) and (c) reveals that pores tend to aggregate in the darker areas, which indicates the presence of pores between deposited layers. As microporosity (with a pore size lower than the resolution of the XCT image is undetectable) is also expected to be present, the lower attenuation in this area is justified. Also, the expected presence of lightweight aluminium oxides justifies the attenuation. The average pores radius is 96.1μm, and the average sphericity (ratio between the surface of a sphere with the same volume as the pore and the surface of the pore) is 0.5 ± 0.1, indicating that both regular and irregular pores are present. Fig.7 (d) and (e) shows the number and percentage of pores in different diameter ranges, indicating that pores with diameters between 0.05 and 0.1 have the highest number. Fig.7 (f) shows the number and percentage of pores under different sphericity ranges. It can be seen that pores were mainly concentrated in the region with sphericity ranging from 0.4 to 0.65, with the highest number of pores occurring in the region with sphericity ranging from 0.45 to 0.5. Box plot distribution of pore diameter and sphericity was showed in Fig.7(g). It can be clearly seen the average values of sphericity and diameter, as well as the data distribution.

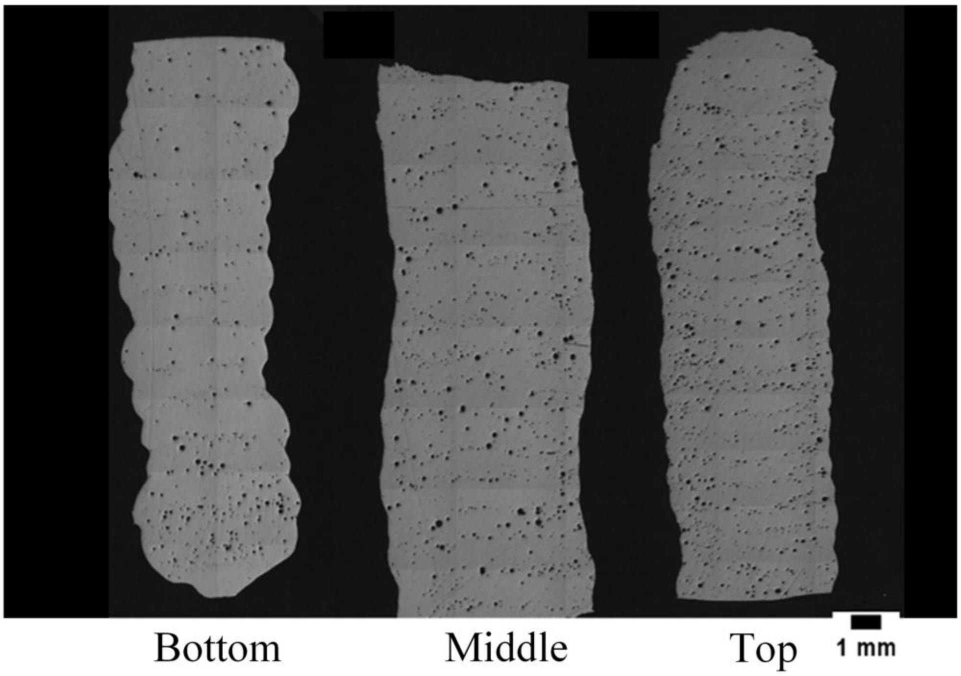

Fig.6 Porosity of three regions of the single strut cross-section by optical microscope: bottom area, middle area and top area

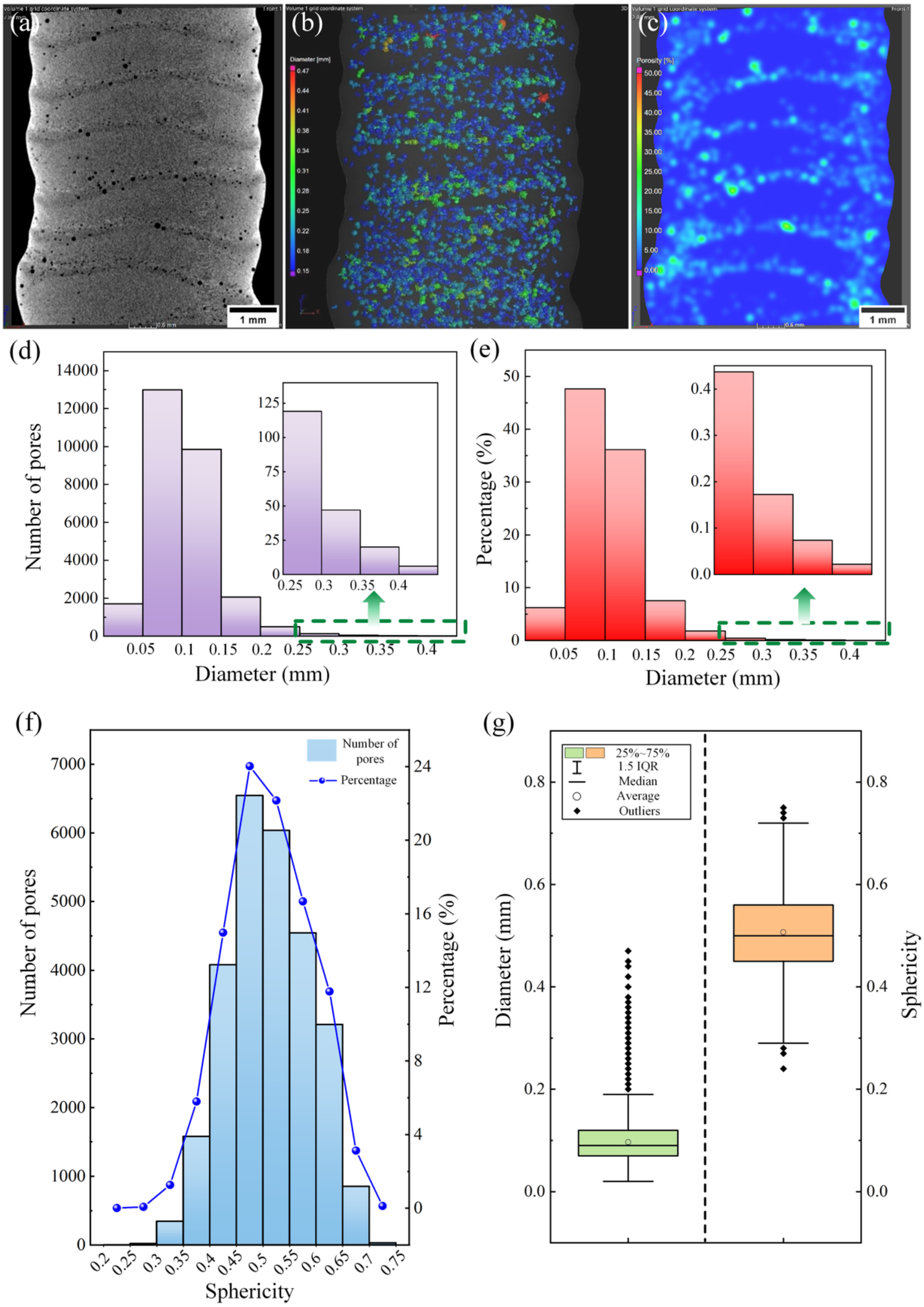

Fig.7 Analysis of porosity by XCT: (a) detail scan of the strut with XCT, (b) Pores identified in the detail image (Only pores with a diameter greater than 0.15 mm are shown), (c) Porosity image (The color represents the percentage of voxels belonging to pores) (d) The number of pores in different diameter regions (e)The percentage of pores under different diameter regions (f) The number and percentage of pores under different sphericity (g) Box plot distribution of pore diameter and sphericity

4.3 Formation mechanism of gas pores

As shown in Fig.7 (b) and (c), the distribution of gas pores followed a certain pattern. Most of the gas pores were distributed along the fusion line of the as-built strut, showing a clear corresponding relationship with Fig.7 (a). According to relevant research, it has been shown that the porosity distribution of aluminium alloy WAAM samples deposited in multiple layers and weld beads mainly occurs in the overlapping areas of the melt bead, but there are also pores in the interlayer area of the aluminium alloy [54-56]. Therefore, the formation and distribution mechanism of gas pores of aluminium alloy struts manufactured by WAAM with dot-by-dot can also be explained by the fluidity of the melt pool and the force analysis on the pores.

Fig. 8 offers a graphical explanation of the formation mechanism of gas pores in dot-by-dot strut. Fig. 8 (a) shows a photo of the solidification of the first melted droplet formed on the substrate during the actual deposition process. Due to the surface tension, the droplet appears spherical on the substrate, and after bonding with the substrate, it becomes the basis for subsequent dot-by-dot deposition. As shown in Fig.8 (b), the build direction (BD) is vertical upwards. The state of the top droplet is shown in Fig.8 (c), and there is supersaturated gas in the melt pool. Grains grow at the bottom of the melt pool. Gas nucleates on the surface of grains because the energy consumed by grain surface nucleation is much lower than that of spontaneous nucleation[57, 58]. Spontaneous nucleation is the initial form of gas pores. After nucleation, pores need to grow under the following conditions (Eq.(1)), as shown in Fig.8 (i).

$$N > 1 + 2F_P R^{-1} \tag{1}$$

where N (N) is the force exerted on the pores by the surrounding liquid, F_P (N/m) is the surface tension between the pore and the liquid, and R (m) is the curvature radius of pores.

After the nucleation of the pore, it grows and moves in the melt pool. The pores move and diffuse with Marangoni convection, and move along the direction of fluid flow, as shown in Fig.8 (c). The difficulty of pore separation is mainly evaluated by the contact angle, as shown (Eq.(2)):

$$\cos\theta = \frac{F_{1,P} - F_{1,L}}{F_P} \tag{2}$$

where θ (°) is the contact angle, $\cos\theta$ is the cosine value of the contact angle. $F_{1,P}$ (N/m) is the surface tension between solidified materials and pores, $F_{1,L}$ (N/m) is the surface tension between melt pool liquids and solidified materials. As shown in Fig.8 (d), the pores continuously move in the melt pool, gradually moving from the bottom to the top of the melt pool. As shown in Fig.8 (e), During the initial movement of the pores, due to the small size, they are subjected to little buoyancy F_B (N), that makes impossible for them to escape from the melt pool solely through buoyancy. During the movement, the pore is also affected by the force F_T (N) of the surrounding fluid and the thermal capillary force f_n (N) caused by the surrounding temperature gradient[57, 58]. During the flow process, $F_B \ll F_T$, $F_B \ll f_n$, so the small pore will continue to move in the melt pool but will not escape[57, 58]. Another part of small pores continuously converges during the flow process, forming larger pores. As shown in Fig.8 (d) some pores will escape from the melt pool at a certain speed under the conditions shown in follows (Eq.(3))[58]:

$$v = \frac{2gR^2}{9\tau}(\rho - \kappa) \tag{3}$$

where v (m/s) is the escape velocity, g (m/s^2) is the gravitational acceleration, R (m) is the curvature radius of pores, τ (N·s/m²) is the viscosity, ρ (N/m³) is the density of liquid, κ (kg/m^3) is the density of gas. In fact, there are still many pores that cannot meet the escape conditions and ultimately remain in the melt pool, becoming gas pores after solidification.

After completing the deposition of the N_{th} layer, the schematic diagram of the deposition of the N_{th+1} layer is shown in Fig.8 (f). In dot-by-dot deposition process, each dot approximates a droplet, and in the manufacturing of struts, a droplet is a layer. When the droplet falls and comes into contact with the deposited material (the N_{th} layer), some of the material remelted, as shown in the Fig.8 (g). At this point, the pores in the solidification area that have not reached the remelting boundary cannot escape. In the remelting area, some new pores are generated and move due to meeting the nucleation conditions, and finally escape. As the melt pool gradually solidifies, the pores that cannot escape also remain in the remelting zone that has already solidified and become gas pores, as shown in the Fig.8 (h). In the subsequent continuous deposition process, multiple remelting zones will always appear, so the internal gas pores of aluminium alloy struts are mainly concentrated near the remelting zone.

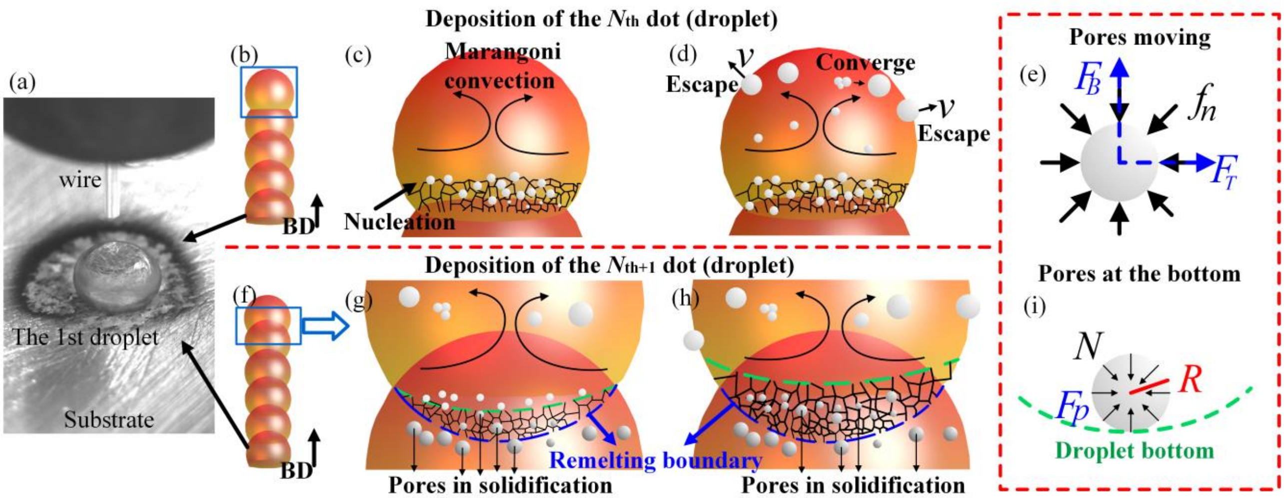

Fig.8 Formation mechanism of gas pores in dot-by-dot strut: (a) first droplet deposited on the substrate, (b) deposition of the *N*th dot, (c) nucleation of pores in melt pool, (d) pores moving, converging and escaping, (e) force analysis of pores moving in melt pool, (f) deposition of the N_{th+1} dot, (g) remelting area in the deposition of the N_{th+1} dot, (h) pores in solidification and in remelting area, (i) force analysis of pores at the bottom of droplet

4.4 Microstructural analysis

Microstructural acquisitions were taken at different regions of the single struts in Fig.9. Fig.9 (a) show the cross-section of the dot-by-dot strut in three areas (the area-bottom, the area-middle and the area-top). Fig.9 (b) ~ (e) display the microstructure at lower magnification, while Fig.9 (f) ~ (h) show the microstructure at higher magnification. Columnar grain structures, aligned parallel to the build direction, were observed in the section nearest to the substrate, as shown in Fig.9 (b), while the grains generally exhibited equiaxed shapes in the middle and top areas, as shown in Fig.9 (c) ~ (e). The average grain sizes of the equiaxed grains were measured using the line intercept method according to ASTM 112, as shown in Table 5. Grain sizes tend to be larger in the bottom region, decreasing in size towards top region.

As shown in Fig.9 (f), the microstructure of the aluminum alloy ER2319 strut manufactured dot-by-dot is composed of α(Al) as the matrix, dissolved with a certain amount of Cu, forming an α(Al) solid solution. In the bottom region, *α*(Al) mainly appears in the form of equiaxed grains, with clear grain boundaries and the presence of a second phase inside the grains, mainly $\theta(Al_2Cu)$. $\theta(Al_2Cu)$ mainly precipitates in eutectic form with *α*(Al), and its size is relatively large, which can be clearly observed inside the grains. The microstructure of the middle region is more irregular in shape compared to the bottom, and there are more second phase distributions at grain boundaries and inside the grains, as shown in Fig.9 (g). As the deposition process continuing, irregular dendritic grains begin to appear in the top area of the strut, and the grain size is uneven, as shown in Fig.9 (h).

The changes in grain morphology and size in different regions of the same strut can be explained by the criterion of constitutional supercooling. Currently, researchers have explored the relationship between supercooling and grain morphology by studying the thin-walled and bulk deposition processes of aluminum alloys [59-61], as shown in Eq. (4).

$$\frac{G}{V} < \frac{Q}{Dk} = \frac{\Delta T}{D} \tag{4}$$

where G (K/m) is the temperature gradient, V (m/s) is the solidification rate, Q is the growth inhibition factor, ΔT is the solidification temperature range, D is the solute diffusion rate. The ratio of G to V has a decisive effect on the morphology of grains. Usually, the larger the ratio of G to V, the grains are columnar grains. If the ratio of G to V is small, the grain morphology is mainly equiaxed. In the initial stage of dot-by-dot process, the melt pool is overlapped and solidified on the substrate, which absorbs a large amount of heat to form a large degree of undercooling. At this time, the G and V are both large. However, compared to the WAAM with thin-wall or bulk deposition, the process of dot-by-dot deposition of strut has a smaller heat input, a smaller temperature gradient, and a relatively faster cooling rate. Therefore, the grains at the bottom appear as columnar grains. As the deposition process progresses, the temperature gradient and cooling rate decrease, resulting in equiaxed grain morphology. In addition, as the dot-by-dot progresses, the melt droplets continue to stack and solidify, and the decrease in temperature gradient and cooling rate can also easily lead to a decrease in the viscosity of the top melt pool. The speed of the pores at the top of the aluminum alloy strut are generated and moved in the melt pool increases (Eq.(3)), and the number of pores increases compared to the initial stage of deposition, resulting in a phenomenon where the porosity in the top region is greater than that in the bottom region during pore observation in Fig.6.

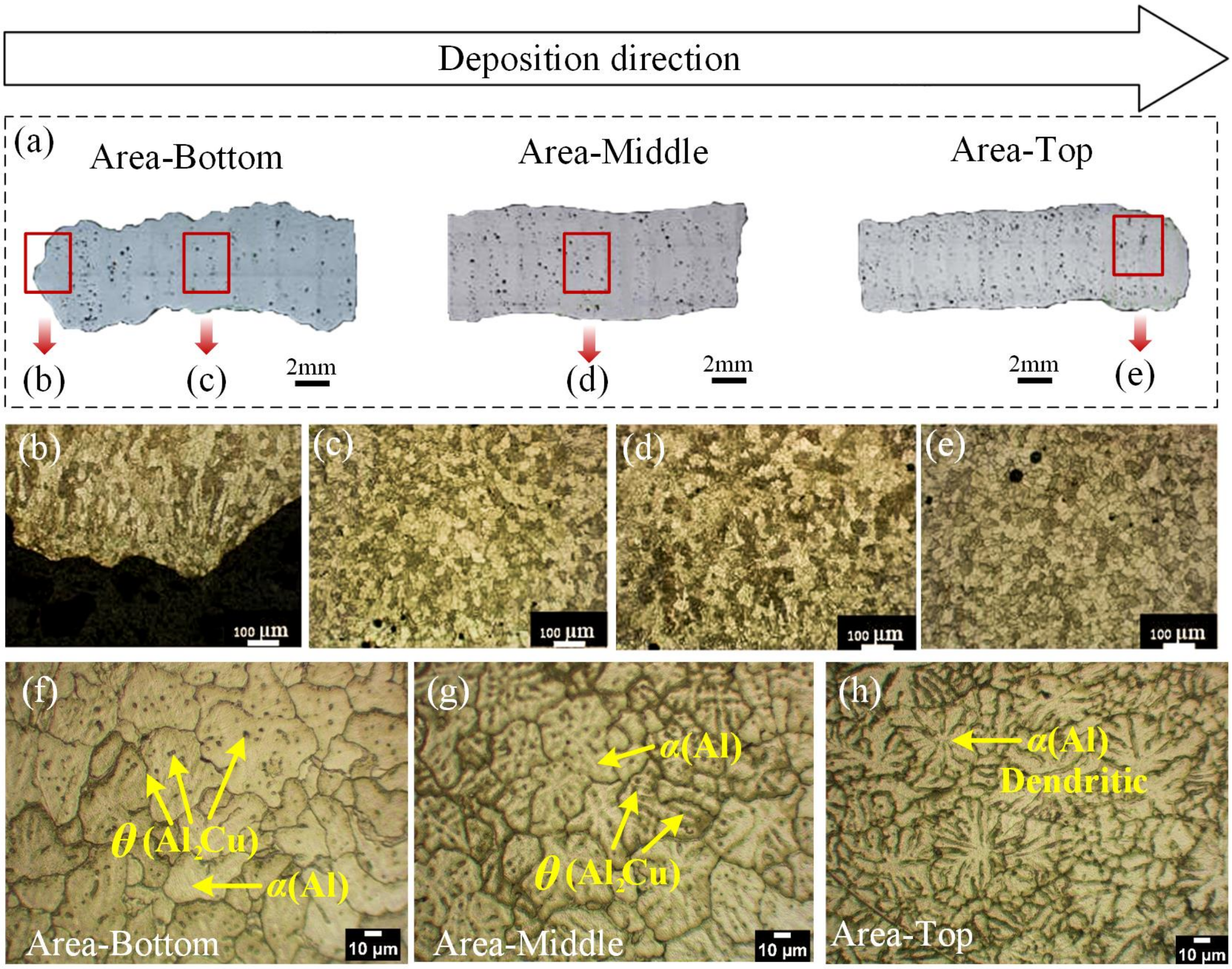

Fig.9: Microstructure at different regions of the single strut: (a) cross-section of the dot-by-dot strut in three areas. (b)~(e) microstructure at lower magnification of areas in Fig.9(a). (f)~(h) Microstructure of areas in different areas (bottom, middle and top)

Table 5: Average grain size of different aeras

	Bottom	Middle	Top
Average grain size (including standard deviation)/μm	24.0±2.9	20.8±1.6	18.4±1.1

4.5 Microhardness and tensile properties

The microhardness measurements of the three sections are shown in Fig.10. The microhardness values exhibited slight variation both between and within each section at different locations, with the overall average being 63 ± 5.5 HV. The microhardness of the top area is the highest, while the microhardness values of the middle and bottom areas are approximately equal. This is due to the presence of numerous Al_2Cu intermetallic compound phases within the grains and at the grain boundaries in the top area, as observed in the microstructure image, which results in a relatively high microhardness. The presence of pores usually reduces the microhardness of as-built aluminum materials. This is because pores reduce the effective load-bearing area of the material and cause stress concentration, weakening the local deformation resistance of the material. The distribution of pores is not completely uniform, so different regions of the material may exhibit differences in microhardness. In some areas, although the porosity is low, the concentrated distribution of pores can still lead to a decrease in microhardness. The formation of pores in aluminum alloy dot-by-dot strut is closely related to manufacturing process parameters. Optimizing process parameters can reduce the generation of pores, thereby improving microhardness. Excessive heat input or scanning speed can easily lead to incomplete or excessive melting, resulting in an increase in porosity and a decrease in microhardness.

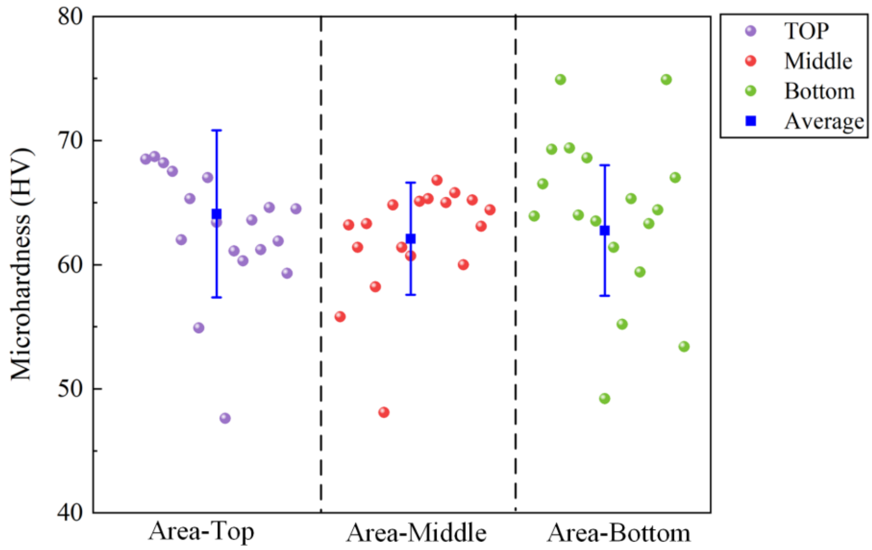

Fig.10 Microhardness of the single strut regions (bottom, top and middle) and comparison with literature

Fig.11 presents the stress-strain plots of the different specimens tested under tensile load, and Fig.11(e) shows the photo of the as-built samples during the tensile experiment. AB-1 ~AB-5 are the as-built tensile samples, while M-1 ~ M-3 are the machined tensile samples. Due to the high variability in the cross-sectional area of the stretched struts typical of the dot-by-dot printing strategy, two different cross-sectional area (the effective area A_{eff} and the minimum area A_{min}) measures were used to assess the stress-strain behavior under tensile loading. Specifically, Fig.11 (a) displays the plots considering the effective cross-sectional A_{eff}, calculated as an equivalent value from volume measures[38, 39]. Conversely, Fig.11 (b) depicts the same plots using the minimum cross-sectional area A_{min} obtained from manual measurements on each strut. Table 6 compares the two different values of cross-sectional area and the corresponding values of ultimate tensile strength (UTS). On average, the minimum cross-sectional area is 15% less than the practical value taken from volume equivalency. Table 7 shows the UTS referred to machined samples. Additionally, Fig.11 (c) reports the stress-strain plot for machined tensile samples. As depicted in Fig.11 (d), the machined samples display higher strength values, indicating a significant detrimental effect of the cross-section irregularity of the as-deposited struts. Due to the inevitable presence of errors in the straightness of the as-deposited rods during the manufacturing process, there were protrusions on the surface of the rod, which can easily lead to stress concentration when subjected to tensile loads, resulting in the actual UTS at fracture being smaller than the standard tensile specimen after processing. In addition, when the as-built sample is clamped onto the tensile testing machine, due to the irregular geometric dimensions of the surface at both ends of the sample, there is no fully compatible fixture compared to the standard tensile specimen. Therefore, further tension loss caused by friction is prone to occur during the tensile process, which is reflected in the final difference in tensile performance, as shown in Fig.11 (e).

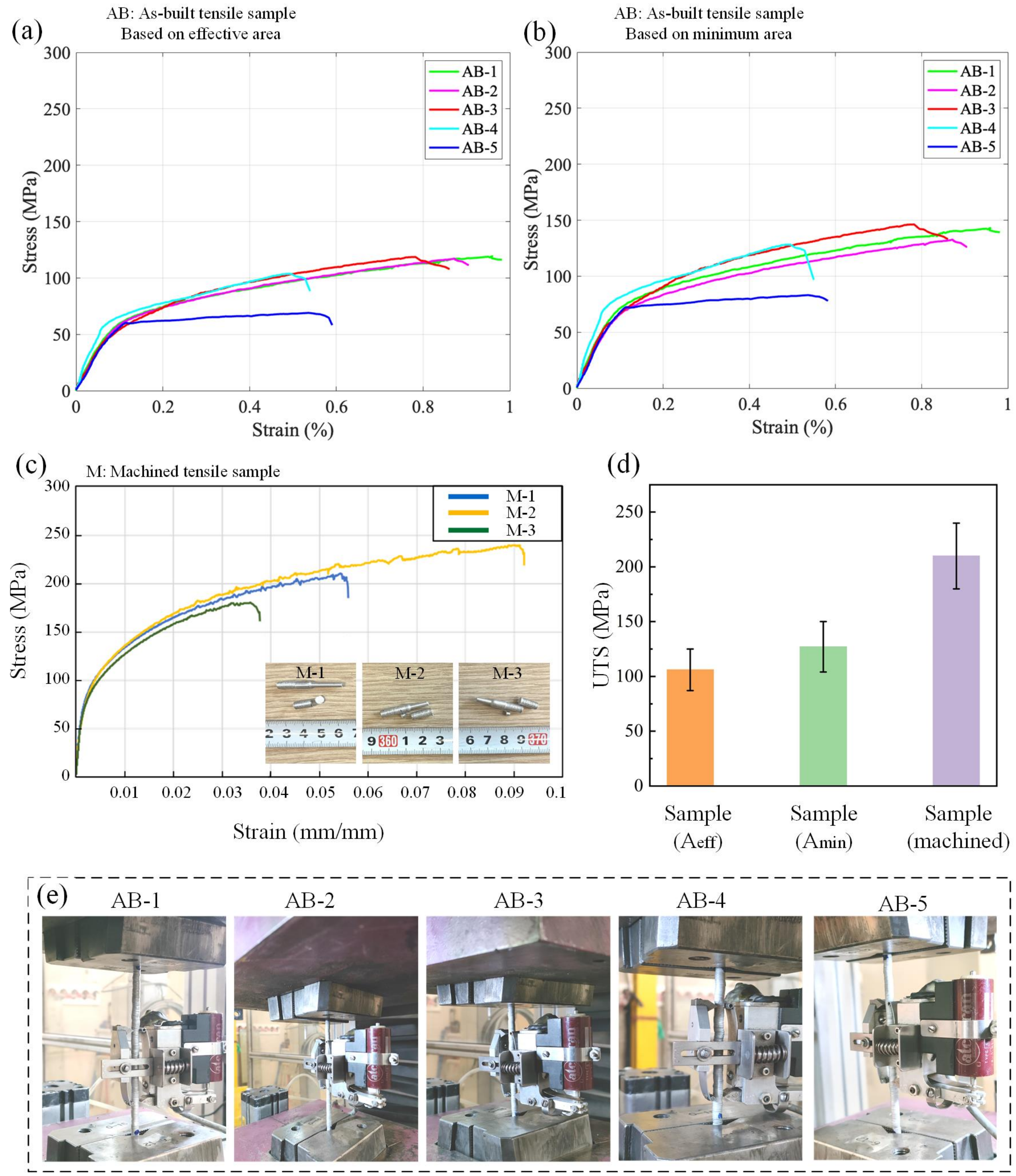

Fig.11 Stress-Strain curves assuming: (a) result of the 5 as-built tensile samples based on the effective area, A_{eff}, (b) the tensile results are recalculated based on minimum area A_{min}, (c) the tensile result and photos of 3 machined tensile samples, (d) comparison of different types of result, (e) photo of the as-built samples

Table 6: Ultimate tensile strength (UTS) refers to each WAAM aluminum bar considering both effective and minimum areas.

Specimen	A_{eff} [mm^2]	A_{min} [mm^2]	A_{min}/A_{eff}	UTS (A_{eff}) [MPa]	UTS (A_{min}) [MPa]
AB-1 (as-built sample)	22.90	19.09	0.83	119	143
AB-2 (as-built sample)	22.99	20.27	0.88	117	133
AB-3 (as-built sample)	23.07	18.70	0.81	119	146
AB-4 (as-built sample)	22.99	18.55	0.81	104	128
AB-5 (as-built sample)	24.37	20.27	0.83	69	83
Average (including standard deviation)	23.26±0.55	19.38±0.75	0.83±0.03	106±19	127±23

Table 7: Ultimate tensile strength (UTS) refers to WAAM aluminum bar (machined sample)

Specimen	UTS [MPa]
M-1 (machined sample)	180.5
M-2 (machined sample)	239.8
M-3 (machined sample)	180.5
Average (including standard deviation)	210.2±29.7

The fracture photos of two types of tensile specimens (as-built sample and machined sample) are shown in the Fig.12. By taking scanning electron microscope (SEM) images of the fracture surface, Fig.12 (a) and (b) show the fracture surface of the as-built sample. It can be seen that the fracture surface has obvious ductile dimples and pore characteristics, indicating that the fracture mode is mainly plastic fracture. Fig.12 (c) and (d) show the fracture surface characteristics of the machined tensile specimen, which are similar to those of the unprocessed fracture surface, and also exhibit more ductile dimples, which is a typical plastic fracture characteristic.

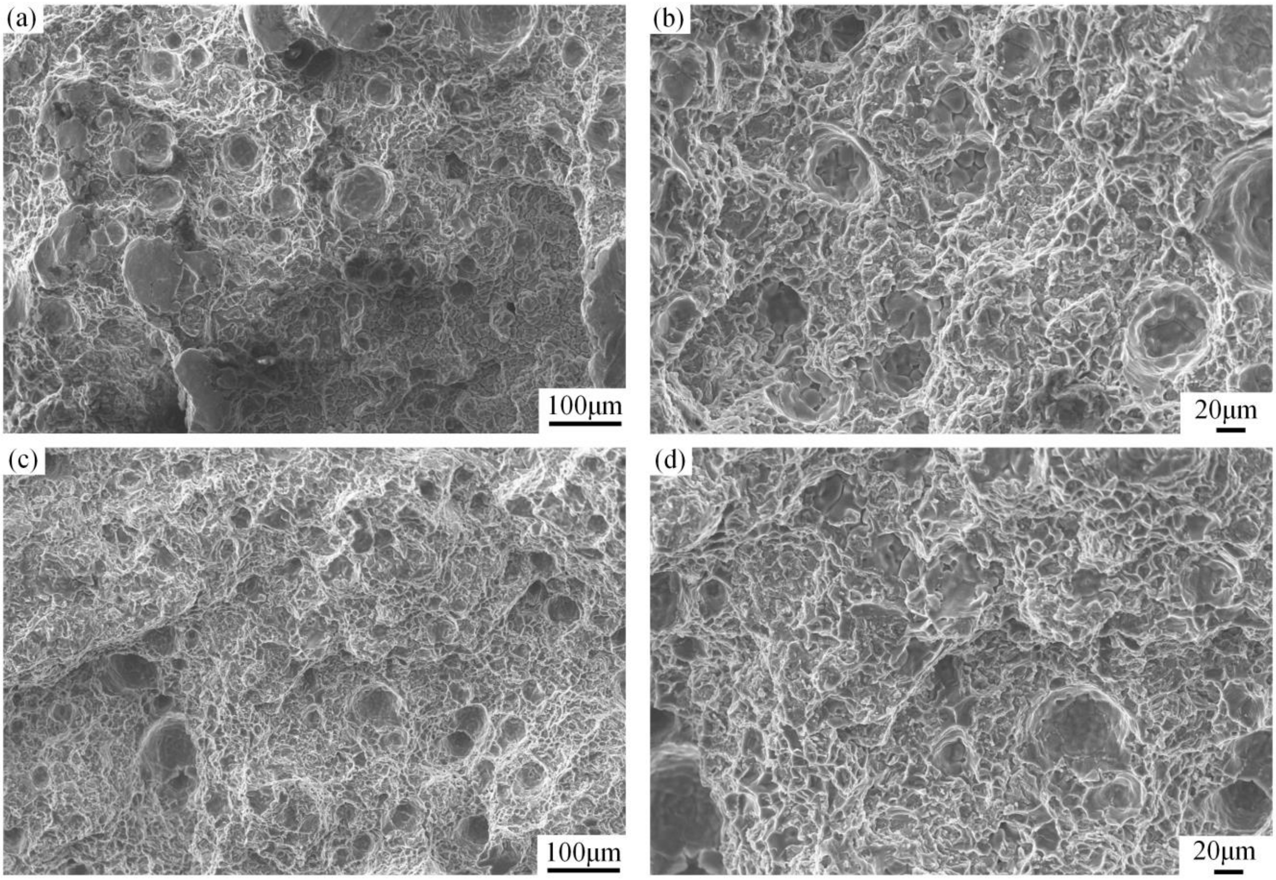

Fig.12 Fracture photos of tensile samples: (a) and (b) photos of as-built strut samples, (c) and (d) photos of machined strut samples

4.6 Deposition strategies for lattice structures

The "X lattice unit", the unit cell of the designed lattice structure was deposited adopting the same WAAM dot-by-dot strategy but employing droplet overlap on the joint, as shown in Fig.13(a). The same set of process parameters as shown in Table 3 and adopted for the strut were also employed for the lattice structures. Primary defects were observed in the deposited lattice unit cell in Fig.13(a). Firstly, the bottom two struts were not joined to each other. Secondly, due to the proximity of the two points of the two struts, a single undesigned and undesired structure was formed after the cross-joint.

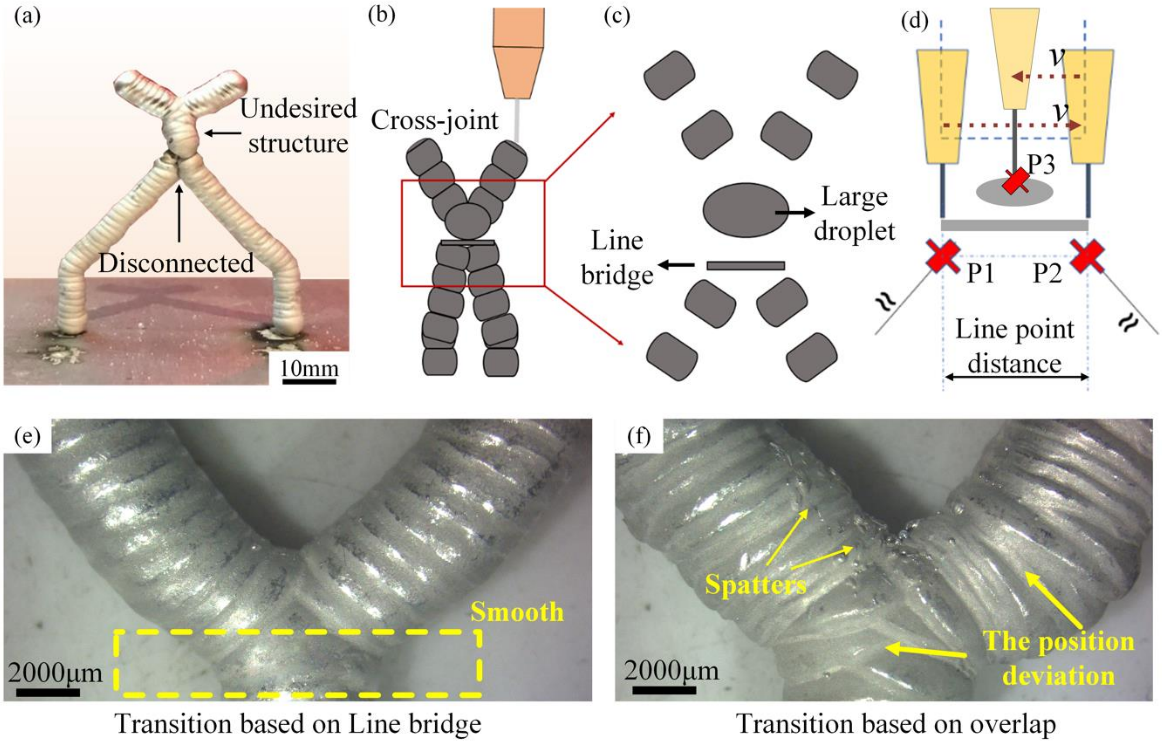

Fig.13 "X lattice unit" design and deposition: (a) single "X lattice unit" deposited with WAAM. (b) redesign of single "X lattice unit", (c) the cross joint of "X lattice unit", (d) schematics of the deposition of the line at the cross joint, (e) cross joint based on line bridge, (f) cross joint based on overlap

In order to solve the deposition issues in the cross-joint area, smooth deposition of cross-joint can be achieved by adjusting and designing dot-by-dot deposition strategies and paths. As shown in Fig.13(b), the strategy of line bridge connection was adopted. This strategy provides a line bridge between the two struts, upon which the diverging struts are deposited, as shown in Fig.13(c). In addition, after the deposition of the line bridge, the welding torch should be moved to the center position to deposit a larger droplet (node) as the foundation for the subsequent two inclined struts, as shown in the Fig.13(c). Therefore, the actual sedimentation strategy for the entire process is shown in the Fig.13(d). Firstly, the welding torch moves linearly at a speed of v from P1 to P2, and then moves to the midpoint P3 of the line bridge for the deposition of large-sized droplets. The cross-joint of lattice cell fabricated by different deposition strategies is shown in the Fig.13(e)~(f). The deposition of the cross-joint area manufactured based on the line bridge strategy is smooth, as shown in Fig.13(e), the deposition quality of the subsequent two inclined struts also has advantages. However, manufacturing defects occurred in the cross-joint area based on overlapping dot-by-dot processes, which affected the subsequent deposition position of the strut, resulting in position deviation, as shown in Fig.13(f). The parameters during the actual manufacturing process for each bead type are shown in the Table 8. The line bridge is 4.6 mm in Fig.13(c). In fact, in order to solve cross joint connection problems, the specific steps of the connection strategy in the line bridge area are as follows, when the horizontal distance between the top of the two inclined rods is 5 ~ 10mm, the robot pose should be adjusted to prepare for depositing the line bridge. Then, by extending the arc on time, ensure that the formed droplet size is larger than that of the depositing strut, the purpose is to avoid the continuous overlapping of small sizes in a short period of time, which ultimately makes it difficult to form a line bridge. When depositing line bridges, it is necessary to ensure that the droplet transition is a short-circuit transition and avoid splashing that affects the deposition quality of the cross joint area. After the deposition of the line bridge is completed, large-sized droplets are used to deposit at the center of the line bridge, which can reinforce the intersection node area to maintain its integrity.

After these preliminary tests, the "X lattice unit" was manufactured as shown in Fig.14. Through the deposition of the line bridge (Fig.14(a)), large-sized droplets (nodes) were deposited at the midpoint of the line bridge (Fig.14(b)), and finally the entire sample was gradually fabricated (Fig.14(c)).

Table 8: Varying process parameters for each bead type.

Varying parameter	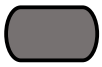		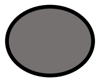
Robot linear speed, v, mm/s	-	5	-
Arc on time, s	0.5	1.3	0.8
Arc wait time, s	10	-	1
Line point distance, mm	-	4.5	-
Nominal Width/Diameter, mm	5	9~10	6

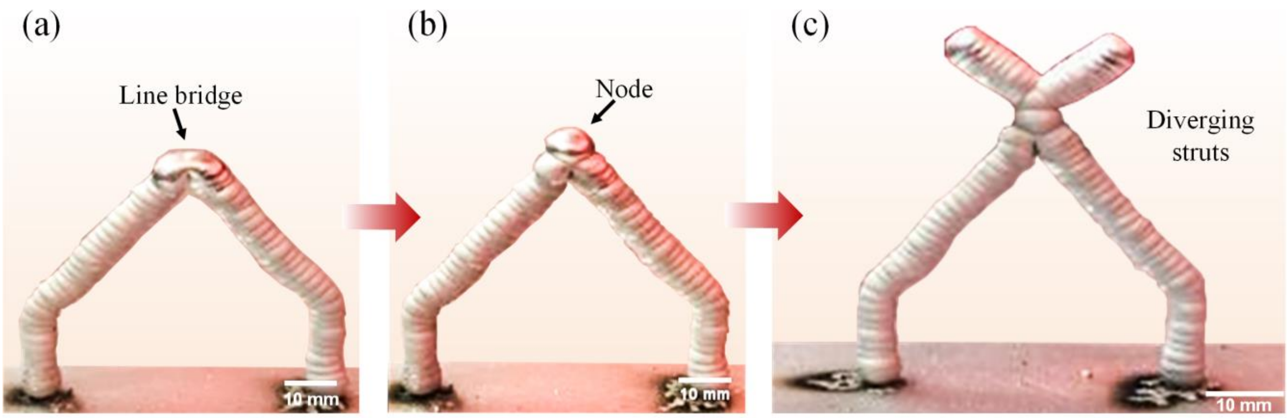

Fig.14 Single "X lattice unit" showing: (a)Line bridge, (b)node dot, (c) diverging struts

The final lattice structure, composed of “X lattice unit” deposited with WAAM dot-by-dot optimized strategy is shown in Fig.15 (a). Porosity analysis was carried out, as shown in Fig.15 (b), revealing that porosity was concentrated just before the inclined rod of the “X lattice unit”. This observation is further confirmed by the detail provided in Fig.15 (c). In the area of the line bridge, the gas pores were clustered and showed a clear regional distribution. The reason for this distribution is attributed to the deposition strategies adopted in the experiment of the line bridge. The specific reasons for the aggregation of gas pores are shown in the Fig.15 (d)~(f). In fact, during the dot-by-dot deposition process, the line bridge can be seen as a lateral stacking of multiple molten droplets, as shown in Fig.15 (d). During the deposition of the first droplet, the growth, flow, and escape of pores inside the melt follow the criteria mentioned in Eq.(1) ~ Eq.(3). However, due to the horizontal building direction (BD) of the line bridge, the direction of the bottom of the melt pool is different from that of the vertical struts, showing a significant inclination, as shown in Fig.15 (e). There are residual gas pores near the bottom boundary of the melt pool that have not escaped, so a more obvious boundary of pore aggregation area can be observed on XCT images, as shown in Fig.15 (c). As the deposition continues along the BD, the second droplet deposits to form a new melt pool, and the range of residual pore aggregation areas move along the BD, as shown in Fig.15 (f), until the line bridge is manufactured.

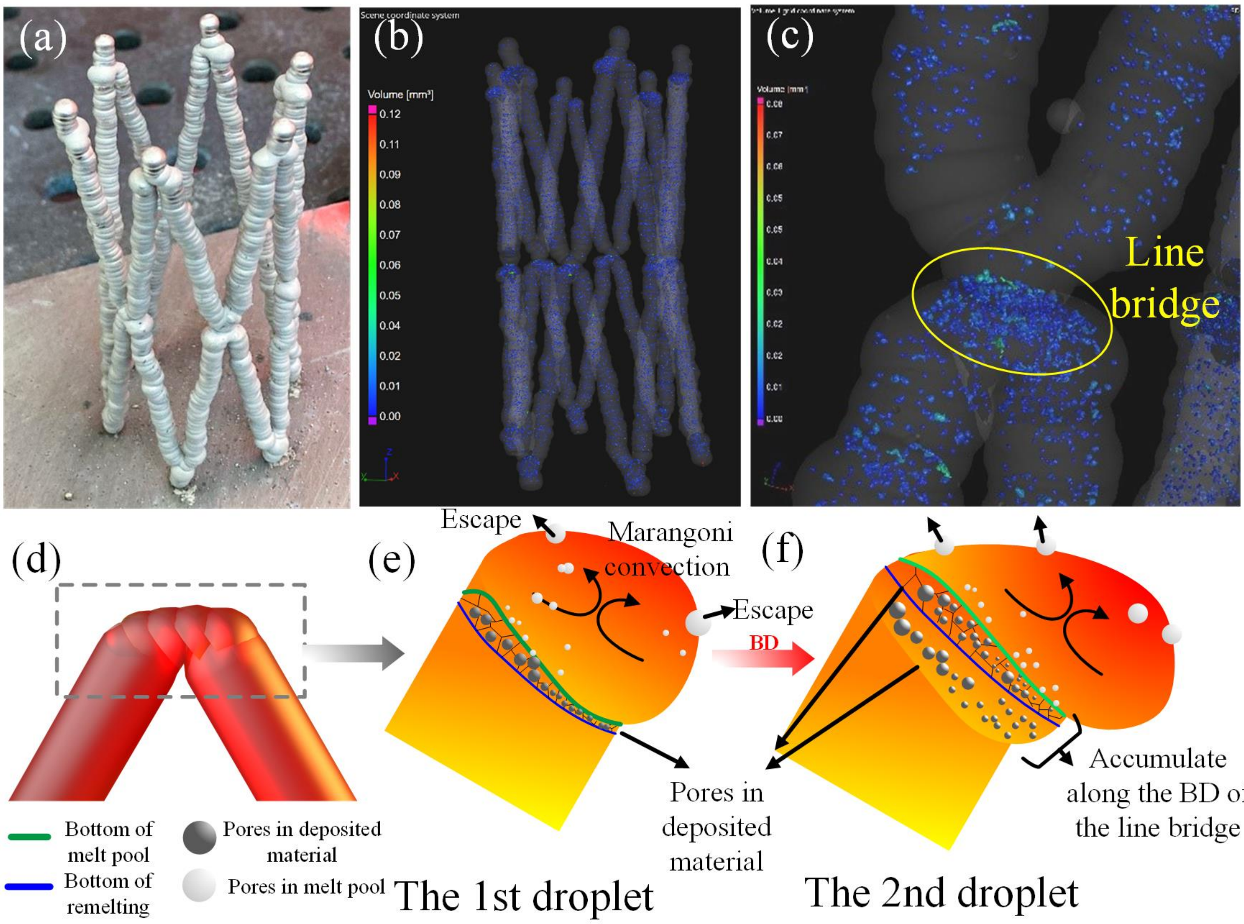

Fig.15 Final aluminum alloy lattice structure deposited with dot-by-dot WAAM. (a) photo of the aluminum alloy lattice structure, (b) Porosity analysis based XCT of lattice structure, (c) XCT enlarged image of the line bridge area, (d) Schematic diagram of deposition in the line bridge area, (e) Schematic diagram of the formation mechanism of pores in the melt pool during the deposition of the first droplet, (f) Schematic diagram of the formation mechanism of pores in the melt pool during the deposition of the second droplet along the BD.

Outlook

This study used dot-by-dot WAAM method to manufacture aluminium alloy strut and lattice structure. This manuscript focused on researching and discussing deposition strategies, processes, internal defect formation mechanisms, and mechanical properties, providing a basic process foundation and case study for the efficient and high-quality manufacturing of dot-by-dot aluminium alloy lattice structures in the future. Future research will further expand on the basis of this study, focusing on the mechanical properties of lattice structures and combining finite element simulation methods to analyse failure modes and compare them with the actual load-bearing capacity of aluminium alloy structures in engineering, in order to further optimize deposition processes.

Conclusions

In this work, the deposition of aluminum (ER 2319) lattice structure by the Wire and Arc Additive Manufacturing (WAAM) process was studied in detail. The porosity, microstructure, and mechanical properties of the lattice structure in its composing elements were studied.

The following conclusions are drawn:

1. Aluminum alloy struts manufactured with WAAM dot-by-dot methods present many internal gas pores, mainly distributed in the interlayer area (remelting zone). The formation mechanism of pores follows the principles of nucleation, growth, flow, and escape. The overall porosity of the single strut considering the three sections is 1.6 ± 0.8 %. The average pores radius is 96.1 μm, and the average sphericity is 0.5 ± 0.1. Pores are mainly concentrated in the region with sphericity ranging from 0.4 to 0.65, with the highest number of pores occurring in the region with sphericity ranging from 0.45 to 0.5.
2. The grain morphology of aluminum alloy struts varies in different regions. The grains in the bottom region are mainly columnar, while the middle and top regions are equiaxed. The microstructure characterization results show that the secondary phases inside the grains of the strut gradually become apparent from the bottom to the top. Microhardness values ranged between 50-75 HV. The higher content of the second phase has an impact on microhardness, while the higher content of the second phase at the top area results in a relatively higher microhardness.
3. Tensile strength was measured for both as-built and machined strut samples. The effective UTS on as-built samples (considering the effective cross-section area) was 106 ± 19 MPa, while the minimum UTS on the same samples (considering the minimum cross-section area) was 127 ± 23 MPa. The UTS of machined samples was 210.2 ± 29.7 MPa, confirming the detrimental effect of the geometrical irregularities proper of the WAAM dot-by-dot process.
4. In order to avoid manufacturing defects when manufacturing “X lattice unit”, a line bridge connection path and deposition strategy were designed. Through experiments, it was confirmed that the line bridge connection process produces better cross-joint node morphology than the original droplet stacking deposition process. Through XCT characterization of the circular lattice structure, it was found that there is a significant accumulation of pores near the line bridge.

Acknowledgments

This work has been partly financed under EU/ERDF measure Tech Fast – Lombardy Region (Italy).

Data availability

All data generated or analyzed during this study are included in this article. All participants state that the contents of the article do not contain unknown, fake or false data.

Ethics declarations

Ethics Approval

This paper does not contain any studies with human participants or animals performed by any of the authors.

Consent to Participate

All of the authors consent to participate.

Consent for Publication

All of the authors consent for publication.

Conflict of Interest

The authors declare that they have no known competing financial interests or personal relationships that could have appeared to influence the work reported in this paper.

Authors' contributions

Luca Baglivo: Investigation, Resources, Writing - Review & Editing. **Giovanni Avallone:** Investigation, Software. **Marco Caso:** Investigation, Resources. **Simone D’Arcangelo:** Investigation, Methodology, Formal analysis, Writing - Review & Editing. **Akshay Ashok Benni:** Formal analysis, Writing - Review & Editing. **Vittoria Laghi:** Writing - Review & Editing, Data Curation. **Lidiana Arrè:** Writing - Review & Editing, Data Curation. **Giada Gasparini:** Writing - Review & Editing, Data Curation. **Michele Palermo:** Writing - Review & Editing, Data Curation. **Stefano Petrò:** Investigation, Writing - Review & Editing. **Tianqiu Xu:** Writing - Original Draft, Writing - Review & Editing, Visualization, Formal analysis. **Barbara Previtali:** Conceptualization, Supervision, Project administration, Writing - Review & Editing.

Reference

[1] S.E. Alkhatib, S. Xu, G. Lu, A. Karrech, T.B. Sercombe, Rate-dependent behaviour of additively manufactured topology optimised lattice structures, Thin-Walled Structures 198 (2024) 111710.

[2] L. Chen, J. Che, S. Liang, Y. Wang, Multiscale topology optimization of gradient lattice structure based on volume parametric modeling, Composite Structures 328 (2024) 117746.

[3] Z. Han, Z. Ma, S. Tong, G. Shen, Y. Sun, J. Li, H. Zhao, L. Ren, Simultaneous enhancements of energy absorption and strength driven by hexagonal close-packed lattice structures of resin revealed by in-situ compression, Thin-Walled Structures 197 (2024) 111586.

[4] B. Li, Y. Shen, W. Hu, Casting defects induced fatigue damage in aircraft frames of ZL205A aluminum alloy – A failure analysis, Materials & Design 32(5) (2011) 2570-2582.

[5] Y.K. Zhang, J.Z. Lu, X.D. Ren, H.B. Yao, H.X. Yao, Effect of laser shock processing on the mechanical properties and fatigue lives of the turbojet engine blades manufactured by LY2 aluminum alloy, Materials & Design 30(5) (2009) 1697-1703.

[6] X.-L. Cui, R. Chu, J. He, C. Han, S. Yuan, Less-loading hydroforming process for large-size hollow components of aluminum alloy, Journal of Materials Research and Technology 15 (2021) 1935-1948.

[7] Y. Li, S. Yu, Y. Chen, R. Yu, Y. Shi, Wire and arc additive manufacturing of aluminum alloy lattice structure, Journal of Manufacturing Processes 50 (2020) 510-519.

[8] Z. Yu, Z. Pan, D. Ding, Z. Rong, H. Li, B. Wu, Strut formation control and processing time optimization for wire arc additive manufacturing of lattice structures, Journal of Manufacturing Processes 79 (2022) 962-974.

[9] F. Guaglione, L. Caprio, B. Previtali, A.G. Demir, Single point exposure LPBF for the production of biodegradable Zn-alloy lattice structures, Additive Manufacturing 48 (2021) 102426.

[10] M. Singh, S. Gusain, S. Kumar Mishra, J. Ramkumar, G. Gomez Escudero, H. Gonzalez Barrio, A. Calleja Ochoa, L. Norberto Lopez de Lacalle, Near-circular EDM hole drilling for deterministic cellular lattice structures of LPBF IN718, Materials Letters 350 (2023) 134886.

[11] Z. Xu, T. Tvenning, T. Wu, N. Razavi, Evaluating quasi-static and fatigue performance of IN718 gyroid lattice structures fabricated via LPBF: Exploring relative densities, International Journal of Fatigue 178 (2024) 108028.

[12] Y. Huang, A.R.O. Wan, K. Schmidt, P. Sefont, S. Singamneni, Z.W. Chen, Effects of cell orientation on compressive behaviour of electron beam powder bed fusion Ti6Al4V lattice structures, Materials Today: Proceedings (2023).

[13] D. Kotzem, T. Arold, K. Bleicher, R. Raveendran, T. Niendorf, F. Walther, Ti6Al4V lattice structures manufactured by electron beam powder bed fusion - Microstructural and mechanical characterization based on advanced in situ techniques, Journal of Materials Research and Technology 22 (2023) 2111-2130.

[14] Z. Zeng, C. Wang, Y.Z. Lek, Y. Tian, S.Y. Kandukuri, P.J.D.S. Bartolo, K. Zhou, Influence of microstructure on stainless steel 316L lattice structures fabricated by electron beam and laser powder bed fusion, Materials Science and Engineering: A 859 (2022) 144225.

[15] T. Abe, H. Sasahara, Layer geometry control for the fabrication of lattice structures by wire and arc additive manufacturing, Additive Manufacturing 28 (2019) 639-648.

[16] Z. Yu, D. Ding, Z. Pan, H. Li, Q. Lu, X. Fang, A strut-based process planning method for wire arc additive manufacturing of lattice structures, Journal of Manufacturing Processes 65 (2021) 283-298.

[17] M. Sharma, H. Dobbelstein, M. Thiele, A. Ostendorf, Laser metal deposition of lattice structures by columnar built-up, Procedia CIRP 74 (2018) 218-221.

[18] C. Chen, T. Feng, Y. Zhang, B. Ren, w. Hao, X. Zhao, Improvement of microstructure and mechanical properties of TC4 titanium alloy GTAW based wire arc additive manufacturing by using interpass milling, Journal of Materials Research and Technology 27 (2023) 1428-1445.
[19] M.D.B. Kumar, N. Arivazhagan, S. Tofil, J. Andersson, J. Kozak, M. Manikandan, Influence of pulsed current GTAW-WAAM process parameters on the single layer bead geometry and multi bead multi-layer deposition of a nickel-based superalloy, Materials Today Communications 39 (2024) 108824.
[20] S.M. Muthu, D. Veeman, A. Vijayakumar, S. Senthur Prabu, S. Sujai, M. Arvind, E. Gobinath, Evaluation of metallurgical and mechanical characteristics of the ferritic stainless steel AISI 430 produced by GTAW-based WAAM, Materials Letters 354 (2024) 135362.
[21] T. Artaza, A. Suárez, M. Murua, J.C. García, I. Tabernero, A. Lamikiz, Wire Arc Additive Manufacturing of Mn4Ni2CrMo Steel: Comparison of Mechanical and Metallographic Properties of PAW and GMAW, Procedia Manufacturing 41 (2019) 1071-1078.
[22] İ. Bayar, M. Ulutan, Investigation of microstructure and mechanical properties of SiC and FeCrC reinforced components fabricated with plasma wire arc additive manufacturing (P-WAAM), Materials Science and Engineering: A 875 (2023) 145115.
[23] C. Sasikumar, R. Oyyaravelu, Mechanical properties and microstructure of SS 316 L created by WAAM based on GMAW, Materials Today Communications 38 (2024) 107807.
[24] W. Zhao, Y. Wei, S. Tashiro, M. Tanaka, A.B. Murphy, Numerical investigations of arc plasma characteristic parameters evolution and metal properties in GMAW-based WAAM of Al alloy with an integrated model, Journal of Manufacturing Processes 99 (2023) 321-337.
[25] D.G. Andrade, T. Tankova, C. Zhu, R. Branco, L.S. da Silva, D.M. Rodrigues, Mechanical properties of 3D printed CMT-WAAM 316 LSi stainless steel walls, Journal of Constructional Steel Research 215 (2024) 108527.
[26] Y. Huang, L. Yang, Q. Xin, Novel geometrical model and design mechanical parameters for CMT-WAAM stainless steel, Journal of Constructional Steel Research 210 (2023) 108071.
[27] Ö.S. Bölükbaşı, T. Serindağ, U. Gürol, A. Günen, G. Çam, Improving oxidation resistance of wire arc additive manufactured Inconel 625 Ni-based superalloy by pack aluminizing, CIRP Journal of Manufacturing Science and Technology 46 (2023) 89-97.
[28] G. Çam, Prospects of producing aluminum parts by wire arc additive manufacturing (WAAM), Materials Today: Proceedings 62 (2022) 77-85.
[29] G. Çam, A. Günen, Challenges and opportunities in the production of magnesium parts by directed energy deposition processes, Journal of Magnesium and Alloys 12(5) (2024) 1663-1686.
[30] F. Ceritbinmez, A. Günen, U. Gürol, G. Çam, A comparative study on drillability of Inconel 625 alloy fabricated by wire arc additive manufacturing, Journal of Manufacturing Processes 89 (2023) 150-169.
[31] B. Cong, J. Ding, S. Williams, Effect of arc mode in cold metal transfer process on porosity of additively manufactured Al-6.3%Cu alloy, The International Journal of Advanced Manufacturing Technology 76(9) (2015) 1593-1606.
[32] A. Günen, U. Gürol, M. Koçak, G. Çam, A new approach to improve some properties of wire arc additively manufactured stainless steel components: Simultaneous homogenization and boriding, Surface and Coatings Technology 460 (2023) 129395.
[33] A. Günen, U. Gürol, M. Koçak, G. Çam, Investigation into the influence of boronizing on the wear behavior of additively manufactured Inconel 625 alloy at elevated temperature, Progress in Additive Manufacturing 8(6) (2023) 1281-1301.
[34] U. Gürol, Y. Altınay, A. Günen, Ö.S. Bölükbaşı, M. Koçak, G. Çam, Effect of powder-pack aluminizing on microstructure and oxidation resistance of wire arc additively manufactured stainless steels, Surface and Coatings Technology 468 (2023) 129742.

[35] Z. Zeng, M. Salehi, A. Kopp, S. Xu, M. Esmaily, N. Birbilis, Recent progress and perspectives in additive manufacturing of magnesium alloys, Journal of Magnesium and Alloys 10(6) (2022) 1511-1541.
[36] B. Bevans, A. Ramalho, Z. Smoqi, A. Gaikwad, T.G. Santos, P. Rao, J.P. Oliveira, Monitoring and flaw detection during wire-based directed energy deposition using in-situ acoustic sensing and wavelet graph signal analysis, Materials & Design 225 (2023) 111480.
[37] I.O. Felice, J. Shen, A.F.C. Barragan, I.A.B. Moura, B. Li, B. Wang, H. Khodaverdi, M. Mohri, N. Schell, E. Ghafoori, T.G. Santos, J.P. Oliveira, Wire and arc additive manufacturing of Fe-based shape memory alloys: Microstructure, mechanical and functional behavior, Materials & Design 231 (2023) 112004.
[38] V. Laghi, M. Palermo, G. Gasparini, T. Trombetti, Computational design and manufacturing of a half-scaled 3D-printed stainless steel diagrid column, Additive Manufacturing 36 (2020).
[39] V. Laghi, M. Palermo, L. Tonelli, G. Gasparini, V.A. Girelli, L. Ceschini, T. Trombetti, Mechanical response of dot-by-dot wire-and-arc additively manufactured 304L stainless steel bars under tensile loading, Construction and Building Materials 318 (2022).
[40] S. Srivatsav, V. Jayakumar, M. Sathishkumar, Recent developments and challenges associated with wire arc additive manufacturing of Al alloy: A review, 3rd International Conference on Materials, Manufacturing and Modelling (ICMMM), Vellore, INDIA, 2021, pp. 8561-8566.
[41] T. Xu, Y. Cui, S. Ma, J. Wang, C. Liu, Exploring the inclined angle limit of fabricating unsupported rods structures by pulse hot-wire arc additive manufacturing, Journal of Materials Processing Technology 295 (2021).
[42] T. Xu, J. Huang, Y. Cui, C. Jing, T. Lu, S. Ma, X. Ling, C. Liu, Exploring a novel panel-core connection method of large size lattice sandwich structure based on wire arc additive manufacturing, Materials & Design 212 (2021).
[43] T. Xu, S. Tang, C. Liu, Z. Li, H. Fan, S. Ma, Obtaining large-size pyramidal lattice cell structures by pulse wire arc additive manufacturing, Materials & Design 187 (2020).
[44] S. Radel, A. Diourte, F. Soulié, O. Company, C. Bordreuil, Skeleton arc additive manufacturing with closed loop control, Additive Manufacturing 26 (2019) 106-116.
[45] V.-A. Silvestru, I. Ariza, J. Vienne, L. Michel, A.M. Aguilar Sanchez, U. Angst, R. Rust, F. Gramazio, M. Kohler, A. Taras, Performance under tensile loading of point-by-point wire and arc additively manufactured steel bars for structural components, Materials & Design 205 (2021).
[46] T. Wang, X. Zhou, H. Zhang, Control of forming process of truss structure based on cold metal transition technology, Rapid Prototyping Journal 28(2) (2021) 204-215.
[47] B. Wu, Z. Pan, Y. Ziping, S. van Duin, H. Li, E. Pierson, Robotic skeleton arc additive manufacturing of aluminium alloy, The International Journal of Advanced Manufacturing Technology 114(9-10) (2021) 2945-2959.
[48] Z. Yu, Z. Pan, D. Ding, J. Polden, F. He, L. Yuan, H. Li, A practical fabrication strategy for wire arc additive manufacturing of metallic parts with wire structures, The International Journal of Advanced Manufacturing Technology 115(9-10) (2021) 3197-3212.
[49] B. Zheng, S. Yu, L. Tang, Y. Shi, Directed energy deposition-arc of aluminum-alloy curved-generatrix-shell pyramid lattice structure, Journal of Manufacturing Processes 84 (2022) 587-599.
[50] B. Zheng, S. Yu, R. Yu, Z. Yu, Microstructure and properties of in situ Al2O3 particle-reinforced aluminium alloy lattice rods fabricated by wire-arc-directed energy deposition, Journal of Materials Processing Technology 327 (2024).

[51] H. Xu, C. Liu, H. Mao, F. Bai, T. Xu, Strengthening nodes to obtain high-strength pyramid lattice structure by using wire arc additive manufacturing method, Journal of Manufacturing Processes 117 (2024) 125-133.
[52] H. Zhang, J. Huang, C. Liu, Y. Ma, Y. Han, T. Xu, J. Lu, H. Fang, Fabricating Pyramidal Lattice Structures of 304 L Stainless Steel by Wire Arc Additive Manufacturing, Materials (Basel) 13(16) (2020).
[53] V. Laghi, V.A. Girelli, G. Gasparini, T. Trombetti, M. Palermo, Investigation on the elastic flexural stiffness of dot-by-dot wire-and-arc additively manufactured stainless steel bars, Engineering Structures 306 (2024).
[54] G. Guo, J. Wei, G. Wu, C. Kang, C. He, Achieving high strength and fatigue performance of wire-arc additive manufactured 6061 aluminum alloy via interlayer friction stir processing and heat treatment, Materials Letters 370 (2024) 136844.
[55] V.L. Jorge, F.R. Teixeira, A. Scotti, F.M. Scotti, E. Siewert, The significance of supplementary shielding in WAAM of aluminium thin walls, Journal of Manufacturing Processes 106 (2023) 520-536.
[56] C. Wang, Z. Jiang, X. Ma, Y. Zhang, P. He, F. Han, Effect of solid solution time on microstructure and corrosion property of wire arc additively manufactured 2319 aluminum alloy, Journal of Materials Research and Technology 26 (2023) 2749-2758.
[57] R. Fu, S. Tang, J. Lu, Y. Cui, Z. Li, H. Zhang, T. Xu, Z. Chen, C. Liu, Hot-wire arc additive manufacturing of aluminum alloy with reduced porosity and high deposition rate, Materials & Design 199 (2021).
[58] M. Yang, Z. Yang, B. Cong, B. Qi, How ultra high frequency of pulsed gas tungsten arc welding affects weld porosity of Ti-6Al-4V alloy, The International Journal of Advanced Manufacturing Technology 76(5-8) (2014) 955-960.
[59] M. Arana, E. Ukar, I. Rodriguez, D. Aguilar, P. Álvarez, Influence of deposition strategy and heat treatment on mechanical properties and microstructure of 2319 aluminium WAAM components, Materials & Design 221 (2022).
[60] Y. Wei, F. Liu, F. Liu, D. Yu, Q. You, C. Huang, Z. Wang, W. Jiang, X. Lin, X. Hu, Effect of arc oscillation on porosity and mechanical properties of 2319 aluminum alloy fabricated by CMT-wire arc additive manufacturing, Journal of Materials Research and Technology 24 (2023) 3477-3490.
[61] L. Zhang, S. Wang, H. Wang, J. Wang, T. Wang, X. Dai, Investigate the effect of arc characteristic on the mechanical properties of 5A56 Al alloy in CMT arc additive manufacturing, CIRP Journal of Manufacturing Science and Technology 40 (2023) 102-113.